THE JOURNAL OF PHYSICAL CHEMISTRY C

ARTICLE

pubs.acs.org/JPCC

Charge Transport Properties of ZnO Nanorod Aggregate Photoelectrodes for DSCs

Kwangsuk Park, Junting Xi, Qifeng Zhang, and Guozhong Cao*

Department of Materials Science and Engineering, University of Washington, Seattle, Washington 98195, United States

Supporting Information

ABSTRACT: Charge transport properties such as electron lifetime (τ_n), electron diffusion coefficient (D_n), and electron diffusion length (L_n) were investigated for the ZnO nanorod aggregate photoelectrodes annealed at different temperatures to understand the effects of structural evolution on the charge transport properties. With an increasing annealing temperature, the ZnO nanorod crystallites in aggregates experienced the structural evolution from individual rods to partially sintered rods and finally spherical large ZnO nanocrystallites, resulting in the appreciable growth of nanocrystallites and the necks between adjacent nanocrystallites and corresponding surface area reduction. Consequently, the charge transport properties in ZnO photoelectrodes were changed accordingly. The charge transport properties like τ_n, D_n, and L_n showed a strong dependence on nano- and microstructures of the photoelectrodes. This study on the correlation between sintered structure and charge transport properties shows that controlled thermal annealing affecting both light harvesting efficiency and charge collection efficiency through the structural evolution of the ZnO nanocrystallites could be a critical factor for high performance of dye-sensitized solar cells (DSCs).

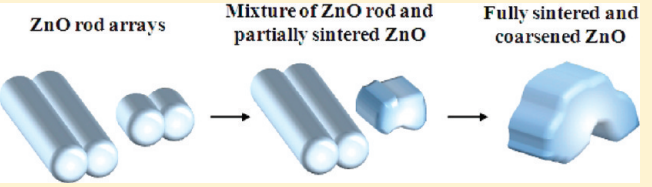

INTRODUCTION

Dye-sensitized solar cells (DSCs) have been intensively studied as a promising alternative to the conventional Si-based solar cells due to the their good features such as low cost and high power conversion efficiency.[1−3] The main component of the DSCs is the photoanode, which is composed of a highly porous semiconducting oxide network on which a close-packed monolayer of dye molecules is formed through surface adsorption. The photons are captured by the dye molecules, and electron−hole pairs are generated. Subsequently, the electrons are injected into the conduction band of the semiconducting oxide and diffuse through the oxide network and, finally, are collected to the anode charge collector, typically FTO glass substrate. At the same time, the oxidized dye molecules are regenerated by electron transfer from iodide ions in the redox electrolyte, and the tri-iodide ions diffuse through the liquid electrolyte to the counter electrode, where they are reduced back to the iodide ions to complete the whole process. In addition to the photon capturing by the dye molecules adsorbed on the oxide that is largely determined by the surface area of the oxide network, the charge transport properties in the oxide network play a crucial role in the power conversion efficiency of DSCs after the electron injection. There are two processes the electrons experience in the oxide network: charge transport and recombination. So, lots of effort has been focused on the determination of electron's lifetime and diffusion coefficient that represent properties of the recombination and charge transport, respectively.[4−6] Also, these two factors could be used to calculate electron diffusion length, L_n, which is an average distance the electrons in the oxide network can diffuse before recombining, so it determines charge collection efficiency, one of the key factors for high performance of DSCs. For efficient charge collection, L_n would be 3 times longer than the thickness of the oxide film.[7]

The nanostructured oxide, which is used to provide huge surface area for high dye loading, is sintered to form the oxide network that acts as a path for charge transport. So, the charge transport behavior would be greatly affected by sintered structures of the nanomaterials. The nanostructured or porous materials are sintered to reduce surface area and finally surface energy, and, generally, the materials become spherical or are fused together to reduce their surface area. As the sintering is a process of time, temperature, and diffusion characteristics of materials, a well-sintered structure for improved charge transport and high performance of DSCs can be possible by controlling these parameters, especially the temperature that is the most powerful factor for the sintering.

ZnO has been studied as a photoelectrode material of DSCs due to its promising characteristics such as easy synthesis process and high electron mobility, and recently lots of progress has been reported.[8−12] One is the layered structure composed of ZnO nanoparticle layer and ZnO scattering layer, followed by the prolonged dye loading time and the decreased distance between the two electrodes.[13] With the comparable photocurrent to the TiO_2-based DSCs, the efficiency over 6% was achieved. The other is ZnO aggregate structure, which allows scattering of incident light within the ZnO film, resulting in increased photon traveling distance and has hierarchical porous structure to minimize

Received: July 14, 2011
Revised: September 19, 2011
Published: September 26, 2011

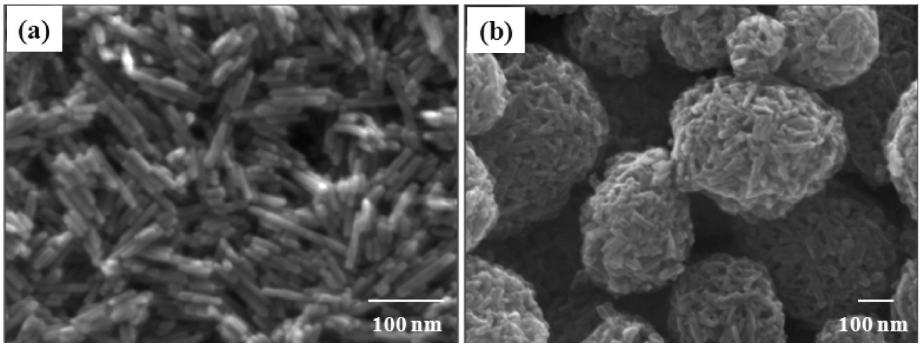

Figure 1. SEM images showing (a) as-grown ZnO nanorods and (b) electrosprayed ZnO nanorod aggregates.

surface area reduction arising from agglomeration of ZnO nanocrystallites.[14] Also, through the application of ALD-TiO_2 layer on this structure, over 6% efficiency was achieved.[15] From the previous work, it was found that the submicrometer-sized aggregate structure can be a good frame in examining the sintering behaviors of ZnO nanocrystallites because one aggregate represents the whole film. Also, as ZnO is a little sensitive to the annealing temperature, various sintered morphologies of ZnO nanocrystallites are possible in a range of 200−450 °C for the annealing.

This Article presents a detailed experimental study on the structural evolution of ZnO rod-shaped nanocrystallites in the form of submicrosized aggregates when annealed at various temperatures ranging from 200 to 450 °C for 1 h in air. Charge transport properties such as electron lifetime, diffusion coefficient, and effective diffusion length were subsequently investigated by electrochemical impedance spectroscopy (EIS), and the relationship between the nano- and microstructures of the photoelectrodes and the charge transport properties has been discussed.

EXPERIMENTAL PROCEDURES

Synthesis of ZnO Nanorods. For ZnO rods preparation, self-assembly of ZnO nanoparticle was used.[16] Zinc acetate dihydrate of 0.01 M was dissolved in 42 mL of methanol with stirring at 60 °C. At the same time, 22 mL of methanol solution dissolving KOH of 0.03 M was prepared under stirring at 60 °C. Once the KOH solution was added into the $ZnO(OAc)_2 \cdot 2H_2O$ solution dropwise, the mixture became cloudy during the addition of the KOH solution and returned to a transparent state within 5 min after completing the addition. After refluxing of 3−5 h at 60 °C, ZnO nanoparticles started to form. ZnO nanorod formation occurred after concentrating the mixture solution 10 times higher by evaporating the solvent. After 1 day, the solution was redispersed in 45 mL of diethylene glycol dissolving $ZnO(OAc)_2 \cdot 2H_2O$ of 0.01 M and heated at 160 °C for 1 h, which is for further rod growth. The ZnO nanorods were separated from the solvent by using a centrifuge at 6000 rpm for 20 min, followed by cleaning with ethanol and drying at 80 °C.

Fabrication of ZnO Nanorod Aggregates. The submicrometer-sized aggregates of ZnO nanorods were fabricated through electrospray. For the electrospray, suspension was made by mixing 0.3 g of ZnO rod with a solution of ethanol (1.2 mL) and distilled water (1.2 mL). For low temperature annealing, an organic material like poly(vinyl pyrrolidone) was not used for the suspension. The ZnO nanorod suspension was electrosprayed with a flow rate of 0.3 mL/h, keeping the distance between the needle tip of syringe containing the ZnO nanorod suspension and the grounded aluminum substrate 17 cm to form an aggregate shape. The applied DC voltage between them was 15 kV. The aggregates were collected on aluminum foil and dried at 100 °C in air for 2 h for further use.

Fabrication of Solar Cells. A drop cast method was used to prepare ZnO film on FTO glass. ZnO nanorod aggregate suspension was made by adding the 0.1 g electrosprayed ZnO nanorod aggregates into 1 g of a solution of ethanol (67%) and distilled water (33%), and a few drops of the suspension were placed on an exposed area of FTO glass, which has already been dammed with a scotch tape. The remained ZnO nanorod aggregate film, after complete evaporation of the solvent, was then annealed at 200, 350, and 450 °C for 1 h in air to get different sintered morphologies of the ZnO aggregates, and the film was controlled with a thickness of 7 μm (see Figure S1 in the Supporting Information). The ZnO nanorod aggregate film then was sensitized by immersing it in 0.3 mM of N719 (Solaronix) for 80 min. The sensitized film was assembled with a Pt-coated silicon, and the gap between two electrodes was filled with electrolyte composed of 0.6 M tetrabutylammomium iodide, 0.1 M lithium iodide, 0.1 M iodine, and 0.5 M 4-tert-butylpyridine in acetonitrile.

Characterization. Surface and cross-sectioned morphologies of the ZnO nanorod aggregate were examined through scanning electron microscopy (SEM). Crystallinity and crystallite size of ZnO nanorods were characterized by means of X-ray diffraction (XRD) with Cu Kα radiation (0.15418 nm). Brunauer−Emmett−Teller (BET, Quantachrome NOVA 4200e) was used to check the surface area variation with annealing temperature. Electrochemical impedance spectroscopy (EIS) study was performed using the Solartron 1287A equipped with the Solartron 1260 FRA/impedance analyzer to measure charge transport properties including electron lifetime, diffusion coefficient, and effective diffusion length under a dark condition. Bias voltage varied from −0.3 to −0.6 to measure charge transfer resistances at the open circuit condition as well as distinguish diffusion resistances from the charge transfer resistances at a second semicircle, keeping the ac amplitude at 10 mV. Frequency applied ranged from 0.05 to 10^5 Hz. The solar cell performances were characterized by using an HP 4155A programmable semiconductor parameter analyzer under AM 1.5 simulated sunlight with the power density of 100 mW cm^{-2}.

RESULTS AND DISCUSSION

Morphologies of ZnO Nanorod Aggregates. Figure 1 shows as-synthesized ZnO nanorods and electrosprayed ZnO rod aggregates used in this work. The as-grown ZnO nanorods seem to have a rather uniform diameter of approximately 10 nm, while

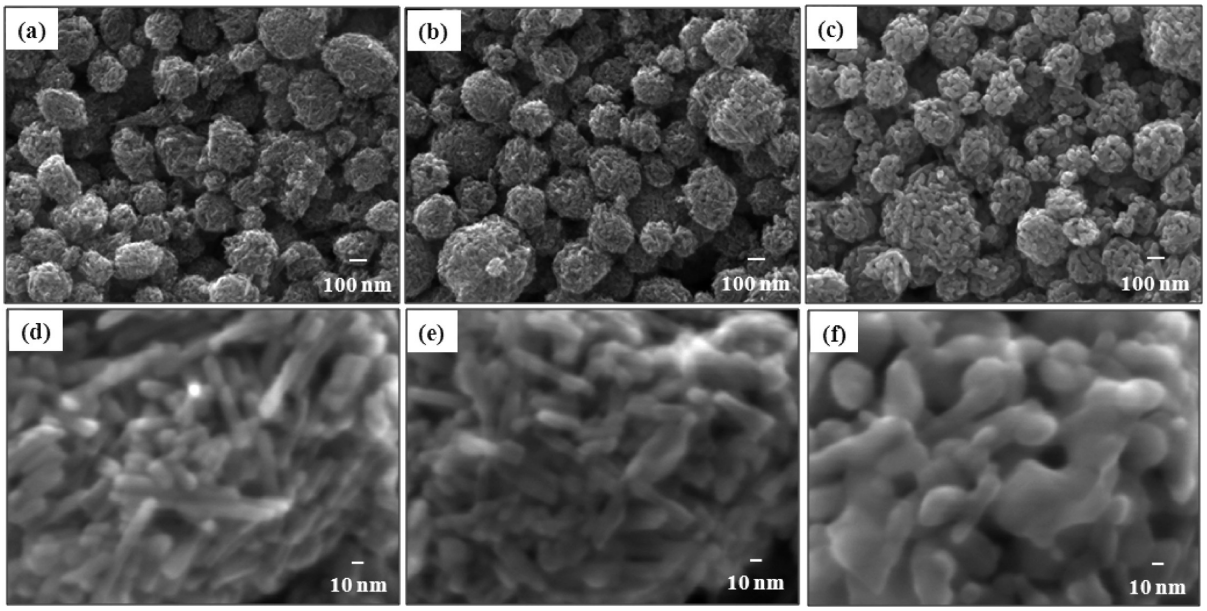

Figure 2. SEM images showing the distribution of aggregates annealed at (a) 200, (b) 350, and (c) 450 °C and the sintered ZnO nanocrystallites annealed at (d) 200, (e) 350, and (f) 450 °C.

their length varies from 30 to 100 nm, and obviously the rod shape of the ZnO remained after forming the aggregate through the electrospray process. The ZnO rod aggregates with diameters of 200−700 nm, even though they are not perfectly spherical, were well-packed. The hierarchical structure of submicrometer-sized aggregates has great advantages for high performance of DSCs, by allowing light scattering as well as retaining their high specific surface area, as demonstrated and reported in the literature.[11,14] In addition, such promising hierarchical structure has another good feature in examining charge transport properties in an oxide network. Because of the inherent complexity and inhomogeneity of a nanoparticle network, it is not easy to simplify the relationship between the structure of a nanoparticle network and charge transport properties occurring in the network. However, in the aggregate film, one sintered aggregate can represent a condition of the whole film for charge transport due to its unique sintering situation.

Figure 2a−c showed the ZnO nanorod aggregate films annealed at 200, 350, and 450 °C; it can be easily inferred that the networking between the aggregates is almost the same even under the different annealing temperatures, indicating that the effect of the connection in the scale of the aggregate on the charge transfer properties can be ignored for different annealing temperatures. The ZnO rod nanocrystallites in the aggregates, however, look to have different sintering experiences with the annealing temperatures as shown in Figure 2d−f. The ZnO rods kept their shape when annealed at 200 °C, and also the rod shape still remained for the annealing at 350 °C. On the other hand, the annealing at 450 °C made the ZnO rod fully sintered and fused together, and, finally, the rod shape of ZnO disappeared.

Such morphology changes were confirmed with the XRD results (shown in Figure 3). The aggregates annealed at 200 and 350 °C showed the comparable intensity of (002) and (101) peaks, although the latter is the highest peak in wurtzite of ZnO, indicating ZnO is in the form of s rod shape corroborating well with the SEM images.

After annealing at 450 °C, ZnO aggregates showed the typical XRD pattern with (101) peak having the highest intensity and (002) peak the lowest, indicating that ZnO nanocrystallites were no longer in the rod-shape, as shown in Figure 2f. The size of ZnO nanocrystallites could be another indicator showing the degree of sintering, because surface diffusion occurs first to reduce surface area at the beginning of sintering at relatively low temperatures, and coarsening as a form of densification at relatively high temperatures follows for further reduction in the surface area of ZnO nanocrystallites. The calculated sizes of the ZnO nanocrystallites annealed at 200, 350, and 450 °C using the Scherrer equation and the intensities of (101) peak are 15.3, 16.7, and 23.9 nm, supporting that the coarsening of the ZnO nanocrystallites occurred with an increasing annealing temperature.[16]

Figure 4a−c shows SEM images of cross-sectioned ZnO nanorod aggregates annealed at 200, 350, and 450 °C for 1 h in air, showing the structural evolution in the ZnO nanorod aggregates under different annealing temperatures. Annealing at 200 °C did not exert any appreciable impact on the rod-shaped ZnO nanocrystallites. However, the ZnO aggregates annealed at 350 °C had a noticeable change in morphology; a mixture of large-sized ZnO nanorods and small fused ZnO nanorods started to be sintered and become spherical, indicating the sintering of the ZnO nanorods starts to occur at 350 °C and from the small-sized ZnO nanorods. The annealing at 450 °C got the ZnO nanorods fully sintered and coarsened, resulting in fused ZnO structures with a spherical shape instead of the rod shape. Schematically, inside aggregate annealed can be denoted as sintered nanocrystallites with different crystal size and neck structures and pores as depicted in Figure 4d. These structural parameters affected by annealing temperature would give a significant impact on charge transport properties of a photoanode in terms of physical and electronic aspects. The enlarged crystal size and neck of the ZnO nanorods would facilitate not only the electron movement but also change the localized states such as bulk trap sites and surface traps sites.

With increasing annealing temperature, it can be concluded that the morphology of the ZnO nanorods evolved as shown in Figure 5, and these structural evolutions from ZnO nanorod

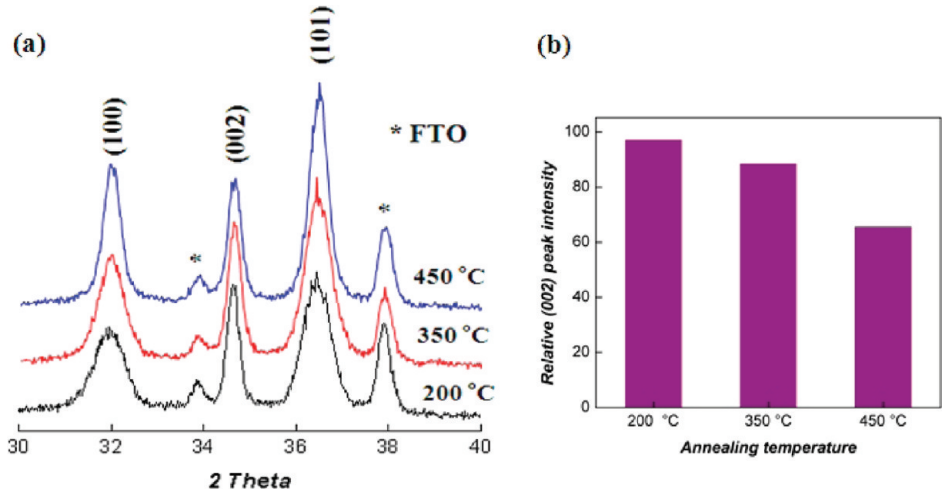

Figure 3. (a) XRD patterns and (b) relative (002) peak intensity to (101) peak of the ZnO nanorod aggregates annealed at 200, 350, and 450 °C.

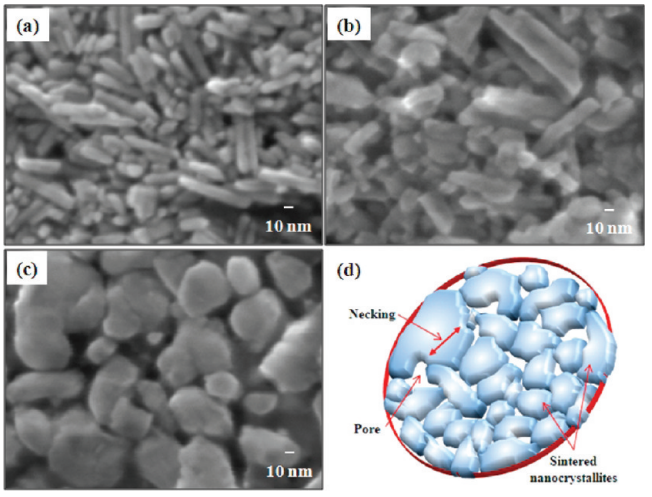

Figure 4. SEM images of the cross-sectioned ZnO nanorod aggregates annealed at (a) 200, (b) 350, and (c) 450 °C and (d) a schematic illustrating the inside structure of the aggregate.

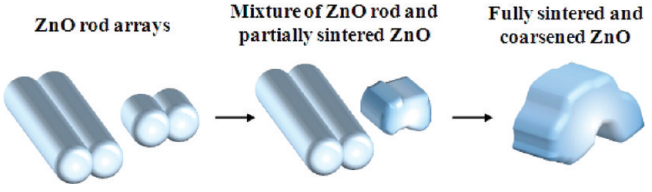

Figure 5. Schematics illustrating the structural evolution of the ZnO nanorods with increasing annealing temperature.

arrays to fully sintered and coarsened ZnO through partially sintered ZnO involve the crystal size and neck growths accompanying with the surface area reduction. Table 1 shows the surface area calculated by the measured nitrogen sorption isotherms using BJH model; the surface area of the ZnO nanorod aggregate was found to decrease with an increasing annealing temperature. The significant reduction of the surface area as much as 27.5% occurred as compared to that of the ZnO nanorod aggregate annealed at 200 °C when annealed at 450 °C, while just

Table 1. Surface Areas Measured by BJH Model for the ZnO Nanorod Aggregates Annealed at 200, 350, and 450 °C

	surface area (m^2/g)
ZnO nanorod aggregate — 200 °C	67.8
ZnO nanorod aggregate — 350 °C	61.3
ZnO nanorod aggregate — 450 °C	49.1

9.5% difference was observed in case of the annealing at 350 °C, supporting the SEM result that the partial sintering for 350 °C annealing and full sintering for 450 °C annealing occurred. On the basis of this structural information, variations of charge transport properties in the ZnO nanorod aggregate films were investigated by EIS and discussed in terms of electron lifetime, diffusion coefficient, and diffusion length in the next section.

Charge Transport Properties. Electrochemical impedance spectroscopy (EIS) is a well-established technique in characterizing DSCs because it shows all kinetic processes of DSCs such as electron transport in an oxide film, recombination property at oxide/electrolyte interface, charge transfer at counter electrode/electrolyte interface, and electron diffusion in an electrolyte.[17−20] Once a bias voltage is applied to DSCs, the electrons are injected into the ZnO aggregate network from a FTO substrate, and the ZnO network gets charged by propagation of the injected electrons. At the same time, some of the injected electrons in the conduction band of ZnO are recombined with I_3^- ions in a redox electrolyte. These processes are denoted as semicircles at different frequency ranges in a Nyquist plot: charge transfer at FTO/ZnO interface over 10^5 Hz, charge transport in the ZnO network and charge transfer at counter electrode/electrolyte interface in the range of 10^5-10^3 Hz, charge transfer at ZnO/electrolyte interface around 10^1 Hz, and ion diffusion in the electrolyte below 10^0 Hz.[19,21,22] The diffusion−recombination model was usually used to analyze these electronic processes. In this model, two basic diffusion theories, the continuity equation and the constitutive equation, combine with a first-order recombination reaction, and the term of electron lifetime is derived as a first-order recombination form of $\tau_e = k^{-1}$, where τ_e is electron lifetime and k^{-1} is kinetic rate constant.[17]

Under the open circuit condition (−0.6 V), a Nyquist plot just displays a charge transfer resistance at the counter electrode/electrolyte interface (R_c) and the ZnO network/electrolyte

dx.doi.org/10.1021/jp2067292 |J. Phys. Chem. C 2011, 115, 20992–20999

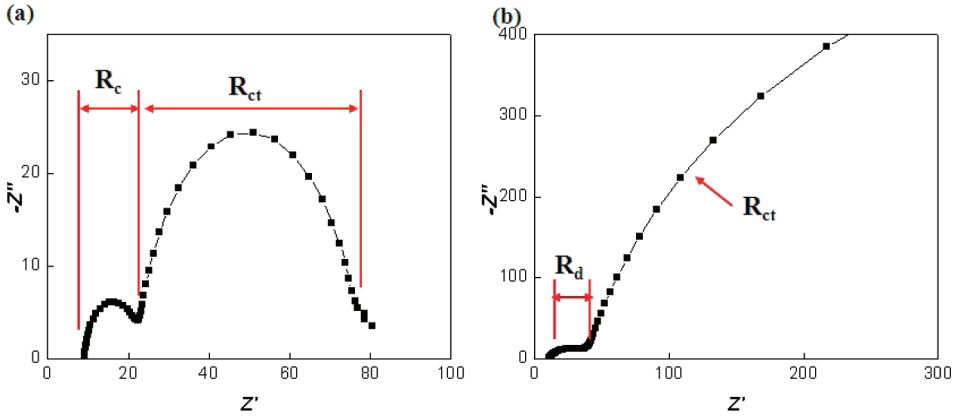

Figure 6. Nyquist plot of the ZnO nanorod aggregates annealed at 200 °C, measured at (a) open circuit condition (−0.6 V) and (b) −0.5 V in which a diffusion resistance (R_d) is shown.

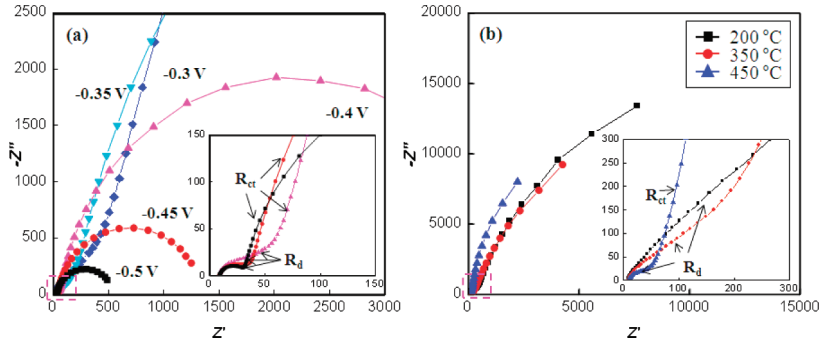

Figure 7. (a) Nyquist plot of the ZnO nanorod aggregates annealed at 200 °C, measured at different bias voltages, and (b) Nyquist plot of the ZnO rod aggregates annealed at 200, 350, and 450 °C, measured at −0.3 V. Insets in (a) and (b) are the enlarged part of the high frequency regions showing that the diffusion resistance (R_d) appeared with reducing bias voltage.

interface (R_{ct}) as shown in Figure 6a. A diffusion resistance (R_d) representing a degree of how effective charge transport occurs by diffusion along with the ZnO network cannot be distinguished from R_c and R_{ct} at this condition because R_d is overlapped with R_c and R_{ct} at the position where transition from R_c to R_{ct} occurs. Yet, with a decrease of the bias voltage from the open circuit condition, a diffusion resistance as Warburg-like diffusion starts to appear with an increase in R_{ct} as shown in Figure 6b. Separating R_d from R_{ct} is useful because charge transport properties such as electron lifetime (τ_n), electron diffusion coefficient (D_n), and diffusion length (L_n) can be calculated by using R_{ct}, R_d, and the corresponding chemical capacitance (C_μ) as follows:[20]

$$\tau_n = R_{ct}C_\mu,\ D_n = \frac{L^2}{R_d C_\mu},\ L_n = \sqrt{\tau_n D_n} \qquad (1)$$

where L is a film thickness. From eq 1, it is obvious that τ_n is relating to the charge transfer resistance, R_{ct} (recombination), while D_n is governed by the charge transport, R_d.

Figure 7 shows how the annealing temperature affects R_{ct}, R_d, and C_μ as components for the charge transport properties. Figure 7a is the Nyquist plot of the ZnO nanorod aggregates annealed at 200 °C, measured by varying the bias voltage from −0.3 to −0.5 V. The R_{ct} known as a shunt resistance showed the exponential decay with the bias voltage.[23,24] At the same time, the straight line as an electron diffusion resistance (R_d) that appeared in the high frequency region of the second semicircle with decreasing bias voltage also showed the exponential dependence on the bias voltage, which can be well-explained by a classical multiple trapping (MT) model.[25] According to the MT model, of the total electron density involving both electrons in the conduction band and electrons in the localized states, the electron transport is slowed by trapping−detrapping events to the localized states, and the localized states distribute exponentially as follows:[26]

$$g(E) = \frac{N_L}{k_B T_0} \exp\left[\frac{E - E_C}{k_B T_0}\right] \qquad (2)$$

where N_L is the total localized trap density, T_0 is a parameter with temperature units that determine the depth of the localized states, E_c is the conduction band energy, and E is the trap energy. With a consideration of the electronic structure for the exponential dependence of R_d on the bias voltage, a physical structure of the film observed in the previous section should be discussed because the film structure also affects the electron movement in the ZnO film. As shown in Figure 7b, the electron diffusion resistance (R_d) was decreased with increasing annealing temperature due to the favorable structural evolutions of ZnO for the charge transport such as the crystal size and neck growths. The lengthened and widened path would enable the movement of electrons to be facilitated through the ZnO network.

R_{ct}, R_d, and C_μ of the ZnO nanorod aggregate films annealed at 200, 350, and 450 °C are plotted in Figure 8. With the exponential dependence on the bias voltage, R_{ct}, R_d, and C_μ were

dx.doi.org/10.1021/jp2067292 |J. Phys. Chem. C 2011, 115, 20992–20999

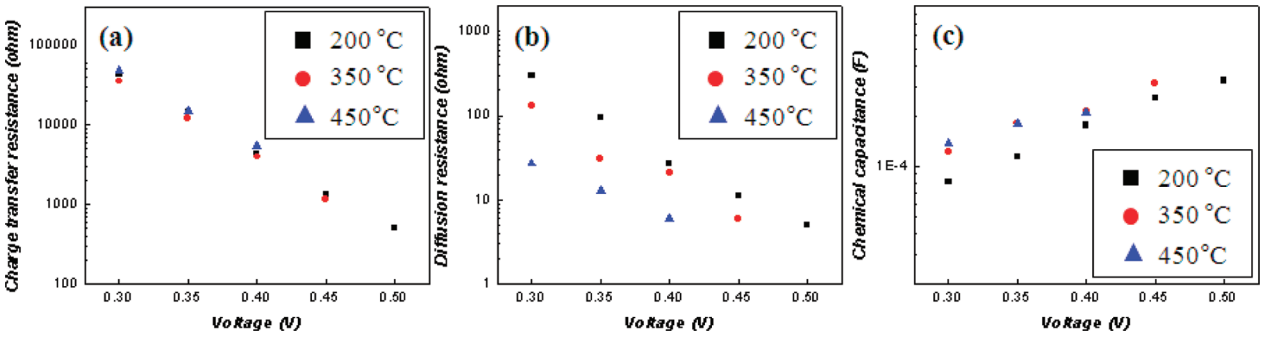

Figure 8. Fitted results of (a) charge transfer resistance, (b) diffusion resistance, and (c) chemical capacitance of the ZnO nanorod aggregates annealed at 200, 350, and 450 °C.

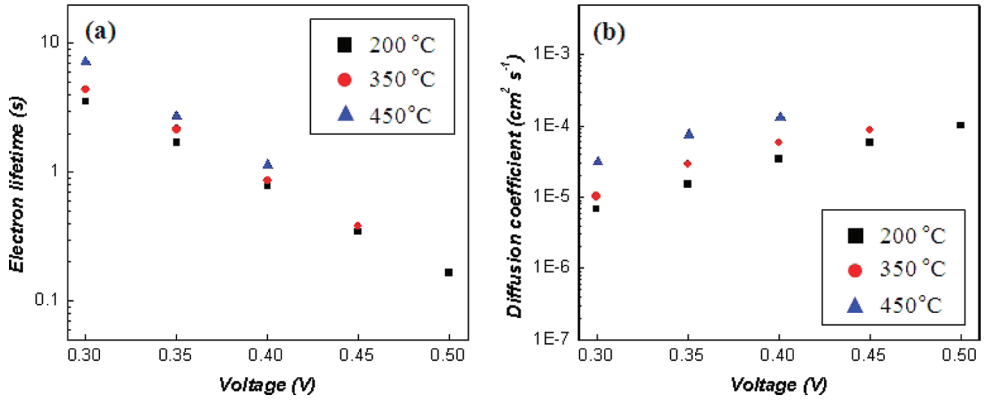

Figure 9. (a) Effective electron lifetime (τ_n) and (b) electron diffusion coefficient (D_n) of the ZnO nanorod aggregates annealed at 200, 350, and 450 °C derived from the combination of the capacitance, R_{ct}, and R_d.

affected by annealing temperatures that led to the structural variations of ZnO nanorods. As charge transfer from the conduction band of ZnO to oxidized species in an electrolyte occurs through the interface between them, the charge transfer resistance, R_{ct}, is directly related to the surface area of the ZnO film. Even the effect of the annealing temperature on R_{ct} was observed as a result of the reduced surface area, and the change in R_{ct} was found to be relatively insignificant as shown in Figure 8a. However, R_d and C_μ were strongly affected by the structural evolution with an increasing annealing temperature, as shown in Figure 8b and c, as increased crystal size and necks would appreciably reduce the charge transport resistance, R_d, by providing the enhanced paths at bottlenecks for electron movement. A chemical capacitance (C_μ) measured by EIS is usually determined by bulk trap sites, not surface trap sites under MT condition like in the range of bias voltage used in the present study ($n_{bulk} \gg n_{surface}$).[27] So, even with the reduction of the surface area that would decrease surface traps occurring with higher annealing temperature, the increased C_μ was observed, suggesting a concentration of bulk traps was increased. The annealing at high temperatures promotes densification of the ZnO nanocrystallites involving neck growth and surface area reduction during the annealing. Bulk traps are likely concentrated at the necks between the adjacent ZnO nanocrystallites and lead to high C_μ.[20] It is also possible that a higher annealing temperature results in a higher concentration of surface oxygen vacancies; however, the contribution of the surface traps to C_μ would be compensated, partially due to the reduced surface area. In Figure 8, the different number of data for each sample was ascribed to the different R_d values of the tested samples (i.e., the R_d of the ZnO nanorod aggregate annealed at 200 °C appeared at −0.5 V due to the highest R_d, while the R_d of the ZnO nanorod aggregate annealed at 450 °C started to be observed at −0.4 V as it has the lowest R_d).

The charge transport properties in DSCs are widely characterized in terms of effective electron lifetime, τ_n, and electron diffusion coefficient, D_n. A variety of methods have been applied to measure them including intensity modulated photovoltage spectroscopy (IMVS) and V_{oc} decay method for τ_n and intensity modulated photocurrent spectroscopy (IMPS) for D_n.[28−30] Electrochemical impedance spectroscopy (EIS) is also widely used for the measurement of τ_n and D_n, and the results of EIS were consistent with the ones of other methods.[18,31] Figure 9a and b shows the calculated τ_n and D_n based on eq 1 with C_μ, R_{ct}, and R_d obtained through EIS (see Table S1 in the Supporting Information). In a quasi-static approximation, effective τ_n and D_n can be expressed simply as follows:[20,32]

$$\tau_n = \left(\frac{\partial n_L}{\partial n_C}\right)\tau_0,\ D_n = \left(\frac{\partial n_C}{\partial n_L}\right)D_0 \qquad (3)$$

where n_C is the density of free electrons, n_L is the density of localized electrons, and τ_0 and D_0 are the lifetime and diffusion coefficient of free electrons. Because of the factor denoting the trapping and detrapping kinetic event, $\partial n_L/\partial n_C$, which contains an exponential characteristic based on eq 2, and τ_n and D_n show strong exponential dependence on the bias voltage as shown in Figure 9. Also, the observed relatively long τ_n (∼second scale)

dx.doi.org/10.1021/jp2067292 |J. Phys. Chem. C 2011, 115, 20992–20999

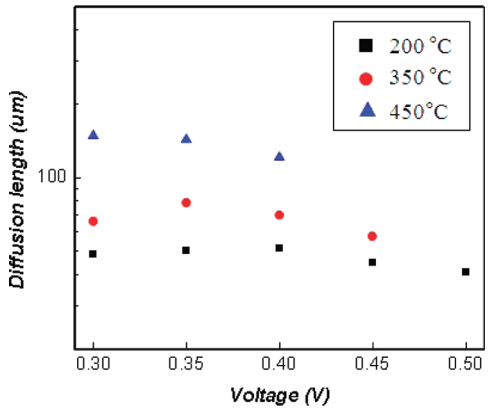

Figure 10. Electron diffusion length of the ZnO nanorod aggregates annealed at 200, 350, and 450 °C calculated by using τ_n and D_n.

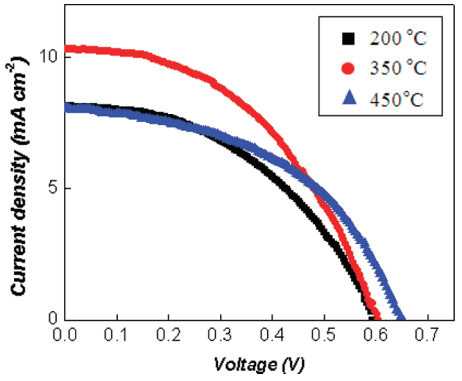

Figure 11. $J-V$ curves of the DSCs with the ZnO nanorod aggregates photoelectrodes annealed at 200, 350, and 450 °C.

and slow D_n (~millisecond scale) indicate the trapping−detrapping event governs them with the condition that the concentration of the localized electrons is much bigger than that of the electrons in the conduction band, $\partial n_L/\partial n_C \gg 1$, in case a trapping−detrapping event makes τ_n and D_n become longer and slower, respectively.[32,33]

Both τ_n and D_n increased with the annealing temperature. The electron lifetime, τ_n, in DSCs commonly refers to the recombination time, instead of a survival time of free electrons. According to eq 1, τ_n is dependent on both R_{ct} and C_μ, a higher annealing temperature increased C_μ, which in turn made τ_n longer. The increase in D_n could be simply explained by the reduction of R_d, charge transport resistance, with increased structural coarsening at higher annealing temperature. Although there was a counter effect of increased C_μ, the reduction in R_d wielded a much significant impact and thus led to enhanced D_n.[34,35] The competing electron transport and recombination processes in the ZnO film could be analyzed and explained in terms of electron diffusion length (L_n) calculated through a relationship $L_n = (\tau_n D_n)^{1/2}$, and the resultant L_n values of the ZnO nanorod aggregates annealed at different temperatures are shown in Figure 10.

The electron diffusion length seems to be little dependent on the bias voltage. When annealed at 450 °C, L_n of the ZnO nanorod aggregate network was longer than 100 μm due to the improved τ_n and D_n, which were ascribed to the structural evolutions of the ZnO nanocrods, in good agreement with that reported in the literature.[7,36] As the electron diffusion length is directly related to the charge collection efficiency, the performance of DSCs was investigated to find out how the improved L_n as a result of the structural evolutions of the ZnO nanorods and corresponding variations of the charge transport properties works, and the performance results are shown in Figure 11 and summarized in Table 2. The highest short circuit current density (J_{sc}) was observed when annealed at 350 °C, while the best open circuit voltage (V_{oc}) was achieved in case of the annealing at 450 °C. The rise in the short circuit current density (J_{sc}) when the annealing temperature was increased from 200 to 350 °C would be ascribed to the improved charge collection efficiency due to the lengthened L_n because at this time, light harvesting efficiency (LHE), another factor determining J_{sc}, would become worse as a result of the reduction of the surface area determining the amount of the adsorbed dye molecules, which would induce a decline of light harvesting efficiency. The effect of the surface area reduction on J_{sc} became dominant for the sample annealed at 450 °C. The remarkable reduction of the surface area (27.5%) that occurred at the annealing at 450 °C would result in the falling-off of J_{sc} even though this annealing condition provided the longest L_n.

Table 2. Performances of the DSCs with the ZnO Nanorod Aggregate Photoelectrodes Annealed at 200, 350, and 450 °C

	V_{oc} [V]	J_{sc} [mA cm^{-2}]	FF [%]	η [%]
ZnO nanorod aggregate − 200 °C	0.594	8.2	47.5	2.32
ZnO nanorod aggregate − 350 °C	0.605	10.3	46.3	2.89
ZnO nanorod aggregate − 450 °C	0.651	8.1	47.6	2.51

On the other hand, the open circuit voltage (V_{oc}) showed different behavior from J_{sc}. The variation of V_{oc} with annealing temperature seems to be similar to the ones of the surface area and electron lifetime: slight change when the annealing temperature increase from 200 to 350 °C and considerable jump for further annealing temperature increase up to 450 °C. It is known that V_{oc} is determined by the potential difference between the Nernstian potential of the electrolyte and the oxide's quasi-Fermi level.[37] So, if the amount of the injected electrons is increased and/or loss of the injected electrons (recombination) is reduced, V_{oc} would increase as a result of the increase in the oxide's quasi-Fermi level. As the recombination occurs through the oxide surface, the reduction of the surface area with annealing temperature would suppress the recombination, leading to the increase in V_{oc}. Even though the variation of the surface area also affects the amount of the injected electrons (amount of the electrons in the conduction band), the recombination seems to exert a critical impact on the determination of V_{oc}. In core−shell systems whose barrier layer usually reduces the recombination as well as electron injection efficiency, the dominant contribution of the recombination to V_{oc} was often observed.[38,39]

CONCLUSIONS

The ZnO nanorods in the aggregates fabricated by means of electrospray have undergone appreciable structural evolutions when subjected to thermal annealing at different temperatures, with the nanorods, partially sintered rods, and fully sintered to coarsen ZnO equiaxial nanoparticles. The structural evolutions involving the crystal size and neck growths and corresponding

surface area reduction with increasing annealing temperature altered the electronic and physical aspects of the ZnO nanorod, exerting significant influences on C_μ and R_d. The increased C_μ and reduced R_d improved τ_n and D_n and, consequently, resulted in a considerable increase in the electron diffusion length (L_n) from 50 to 140 μm. The improved L_n with annealing temperature increased the short circuit current density and finally led to 25% enhancement in the power conversion efficiency of DSCs, despite the surface area reduction.

■ ASSOCIATED CONTENT

Supporting Information. SEM image of the cross-sectioned film showing a film thickness, BET isotherm graph, equivalent circuit used to fit the Nyquist plot, and fitted results on C_μ, R_{ct}, and R_d. This material is available free of charge via the Internet at http://pubs.acs.org.

■ AUTHOR INFORMATION

Corresponding Author
*E-mail: gzcao@u.washington.edu.

■ ACKNOWLEDGMENT

Most of the syntheses of nanostructures and electrical characterization was supported by the National Science Foundation (DMR-1035196) (K.P.), and some detailed structural characterization has been supported in part by the U.S. Department of Energy, Office of Basic Energy Sciences, Division of Materials and Engineering under Award No. DE-FG02-07ER46467 (Q.Z.). J.X. would also like to acknowledge a fellowship from the China Scholarship Council.

■ REFERENCES

(1) Nazeeruddin, M. K.; Kay, A.; Rodicia, I.; Humphry-Baker, R.; Muller, E.; Liska, P.; Vlachopoulos, N.; Grätzel, M. *J. Am. Chem. Soc.* **1993**, *115*, 6382.
(2) Grätzel, M. *J. Photochem. Photobiol., C* **2003**, *4*, 145.
(3) Zhang, Q. F.; Cao, G. Z. *Nano Today* **2011**, *6*, 91.
(4) Quintana, M.; Edvinsson, T.; Hagfeldt, A.; Boschloo, G. *J. Phys. Chem. C* **2007**, *111*, 1035.
(5) Fabregat-Santiago, F.; Canadas, J. G.; Palomares, E.; Clifford, J. N.; Haque, S. A.; Durrant, J. R.; Garcia-Belmonte, G.; Bisquert, J. *J. Appl. Phys.* **2004**, *96*, 6903.
(6) Han, L.; Koide, N.; Chiba, Y.; Mitate, T. *Appl. Phys. Lett.* **2004**, *84*, 2433.
(7) Jennings, J. R.; Ghicov, A.; Peter, L. M.; Schmuki, P.; Walker, A. B. *J. Am. Chem. Soc.* **2008**, *130*, 13364.
(8) Keis, K.; Magnusson, E.; Lindström, H.; Lindquist, S.-E.; Hagfeldt, A. *Sol. Energy Mater. Sol. Cells* **2002**, *73*, 51.
(9) Lai, Y.-H.; Lin, C.-Y.; Chen, H.-W.; Chen, J.-G.; Kung, C.-W.; Vittal, R.; Ho, K.-C. *J. Mater. Chem.* **2010**, *20*, 9379.
(10) Martinson, A. B. F.; Elam, J. W.; Hupp, J. T.; Pellin, M. J. *Nano Lett.* **2007**, *7*, 2183.
(11) Chou, T. P.; Zhang, Q. F.; Fryxell, G. E.; Cao, G. Z. *Adv. Mater.* **2007**, *19*, 2588.
(12) Zhang, Q. F.; Dandeneau, C. S.; Zhou, X. Y.; Cao, G. Z. *Adv. Mater.* **2009**, *21*, 4087.
(13) Saito, M.; Fujihara, S. *Energy Environ. Sci.* **2008**, *1*, 280.
(14) Zhang, Q. F.; Chou, T. P.; Russo, B.; Jenekhe, S. A.; Cao, G. Z. *Angew. Chem., Int. Ed.* **2008**, *47*, 2402.
(15) Park, K.; Zhang, Q. F.; Garcia, B. B.; Zhou, X. Y.; Jeong, Y.-H.; Cao, G. Z. *Adv. Mater.* **2010**, *22*, 2329.
(16) Pacholski, C.; Kornowski, A.; Weller, H. *Angew. Chem., Int. Ed.* **2002**, *41*, 1188.
(17) Bisquert, J. *J. Phys. Chem. B* **2002**, *106*, 325.
(18) Kern, R.; Sastrawan, R.; Ferber, J.; Stangl, R.; Luther, J. *Elecrochim. Acta* **2002**, *47*, 4213.
(19) Hoshikawa, T.; Kikuchi, R.; Eguchi, K. *J. Electroanal. Chem.* **2006**, *588*, 59.
(20) Wang, Q.; Ito, S.; Grätzel, M.; Fabregat-Santiago, F.; Mora-Seró, I.; Bisquert, J.; Bessho, T.; Imai, H. *J. Phys. Chem. B* **2006**, *110*, 25210.
(21) Wang, Q.; Moser, J. E.; Grätzel, M. *J. Phys. Chem. B* **2005**, *109*, 14945.
(22) Fabregat-Santiago, F.; Bisquert, J.; Garcia-Belmonte, G.; Boschloo, G.; Hagfeldt, A. *Sol. Energy Mater. Sol. Cells* **2005**, *87*, 117.
(23) Koide, N.; Islam, A.; Chiba, Y.; Han, L. *J. Photochem. Photobiol., A* **2006**, *182*, 296.
(24) Nakade, S.; Kanzaki, T.; Wada, Y.; Yanagida, S. *Langmuir* **2005**, *21*, 10803.
(25) Tiedje, T.; Rose, A. *Solid State Commun.* **1981**, *37*, 49.
(26) Jongh, P. E.; Vanmaekelbergh, D. *Phys. Rev. Lett.* **1996**, 3427.
(27) Bisquert, J.; Fabregat-Santiago, F.; Mora-Seró, I.; Garcia-Belmonte, G.; Giménez, S. *J. Phys. Chem. C* **2009**, *113*, 17278.
(28) O'Regan, B. C.; Lenzman, F. *J. Phys. Chem. B* **2004**, *108*, 4342.
(29) Zaban, A.; Greenshtein, M.; Bisquert, J. *ChemPhysChem* **2003**, *4*, 859.
(30) Nakade, S.; Saito, Y.; Kubo, W.; Kitamura, T.; Wada, Y.; Yanagida, S. *J. Phys. Chem. B* **2003**, *107*, 8607.
(31) Ponomarev, E. A.; Peter, L. M. *J. Electroanal. Chem.* **1997**, *397*, 45.
(32) Bisquert, J.; Vikhrenko, V. S. *J. Phys. Chem. B* **2004**, *108*, 2313.
(33) Bisquert, J.; Zaban, A.; Greenshtein, M.; Mora-Seró, I. *J. Am. Chem. Soc.* **2004**, *126*, 13350.
(34) Archana, P. S.; Jose, R.; Vijila, C.; Ramakrishna, S. *J. Phys. Chem. C* **2009**, *113*, 21538.
(35) Shi, Y. T.; Dong, H. P.; Wang, L. D.; Zhan, C.; Gao, R.; Qiu, Y. *J. Mater. Chem.* **2011**, *21*, 3183.
(36) Krüger, J.; Plass, R.; Grätzel, M.; Cameron, P. J.; Peter, L. M. *J. Phys. Chem. B* **2003**, *107*, 7536.
(37) Hamann, T. W.; Jensen, R. A.; Martinson, A. B. F.; Ryswyk, H. V.; Hupp, J. T. *Energy Environ. Sci.* **2008**, *1*, 66.
(38) Park, K.; Zhang, Q. F.; Garcia, B. B.; Cao, G. Z. *J. Phys. Chem. C* **2011**, *115*, 4927.
(39) Palomares, E.; Clifford, J. N.; Haque, S. A.; Lutz, T.; Durrant, J. R. *J. Am. Chem. Soc.* **2003**, *125*, 475.